Faraday Discussions

Cite this: DOI: 10.1039/d3fd00171g

ROYAL SOCIETY OF CHEMISTRY

PAPER

View Article Online
View Journal

Open Access Article. Published on 20 May 2024. Downloaded on 5/21/2024 8:27:22 AM.
This article is licensed under a Creative Commons Attribution 3.0 Unported Licence.

Dynamics of carbene formation in the reaction of methane with the tantalum cation in the gas phase†

Marcel Meta, [a] Maximilian E. Huber, [a] Maurice Birk, [a] Martin Wedele, [a] Milan Ončák [b] and Jennifer Meyer *[a]

Received 14th December 2023, Accepted 28th February 2024
DOI: 10.1039/d3fd00171g

The controlled activation of methane has drawn significant attention throughout various disciplines over the last few decades. In gas-phase experiments, the use of model systems with reduced complexity compared to condensed-phase catalytic systems allows us to investigate the intrinsic reactivity of elementary reactions down to the atomic level. Methane is rather inert in chemical reactions, as the weakening or cleavage of a C–H bond is required to make use of methane as C_1-building block. The simplest model system for transition-metal-based catalysts is a mono-atomic metal ion. Only a few atomic transition-metal cations activate methane at room temperature. One of the most efficient elements is tantalum, which forms a carbene and releases molecular hydrogen in the reaction with methane: $Ta^+ + CH_4 \rightarrow TaCH_2^+ + H_2$. The reaction takes place at room temperature due to efficient intersystem crossing from the quintet to the triplet surface, *i.e.*, from the electronic ground state of the tantalum cation to the triplet ground state of the tantalum carbene. This multi-state reactivity is often seen for reactions involving transition-metal centres, but leads to their theoretical treatment being a challenge even today. Chemical reactions, or to be precise reactive collisions, are dynamic processes making their description even more of a challenge to experiment and theory alike. Experimental energy- and angle-differential cross sections allow us to probe the rearrangement of atoms during a reactive collision. By

[a]*RPTU Kaiserslautern-Landau, Fachbereich Chemie und Forschungszentrum OPTIMAS, Erwin-Schrödinger Str. 52, 67663 Kaiserslautern, Germany. E-mail: jennifer.meyer@chem.rptu.de; Fax: +49 631 205 2750; Tel: +49 631 205 4211*

[b]*Universität Innsbruck, Institut für Ionenenphysik und Angewandte Physik, Technikerstr. 25, 6020 Innsbruck, Austria*

† Electronic supplementary information (ESI) available: Fig. S1: reaction coordinate for $Ta^+ + CH_4$ including stationary points of lower importance. Fig. S2: internal energy distributions. Fig. S3: direct comparison of internal and $TaCH_2^+$ energy distributions and mean values of the respective distributions. Fig. S4: velocity distribution for $Ta^+ + CH_4$ at $E_{rel} \approx 1.0$ eV for selected reactant ion velocity subsets. Fig. S5: graphical error representation of product ion velocity distribution. Table S1: time-of-flight values for species of interest. Table S2: benchmarking relative energies (in eV) for three multiplicities in $[TaCH_4]^+$. Table S3: benchmarking of reaction energies (in eV) including Ta–H and Ta–C bonds. Cartesian coordinates and energies for optimized structures for $Ta^+ + CH_4$. See DOI: **https://doi.org/10.1039/d3fd00171g**

Open Access Article. Published on 20 May 2024. Downloaded on 5/21/2024 8:27:22 AM.
This article is licensed under a Creative Commons Attribution 3.0 Unported Licence.

interpreting the scattering signatures, we gain insight into the atomistic mechanisms and can move beyond stationary descriptions. Here, we present a study combining collision energy dependent experimentally measured differential cross sections with *ab initio* calculations of the minimum energy pathway. Product ion velocity distributions were recorded using our crossed-beam velocity map imaging experiment dedicated to studying transition-metal ion molecule reactions. $TaCH_2^+$ velocity distributions reveal a significant degree of indirect dynamics. However, the scattering distributions also show signatures of rebound dynamics. We compare the present results to the oxygen transfer reaction between Ta^+ and carbon dioxide, which we recently studied.

1 Introduction

Methane CH_4 as a major natural carbon feedstock is currently primarily used as fuel, but methane is also a valuable C_1-feedstock for the chemical industry as natural oil resources diminish over the next few decades. However, the effective chemical conversion of methane comes with the challenge of selective activation and chemical modification of methane. CH_4 is chemically rather inert, with one of the strongest C–H bonds, *i.e.*, a bond dissociation energy (BDE) of 4.5 eV.[1] Additionally, it has no dipole moment, no appreciable quadrupole moment, a very low polarizability (2.593 $Å^3$),[1] and an ionization energy of 12.6 eV.[2] All this makes methane practically inert in chemical reactions and necessitates the use of catalysts for economical chemical transformations. Herein lies the challenge of selectivity: at least one chemical bond in most reaction products is more reactive than the C–H bond in methane, which makes the selective activation of methane an ongoing field of research across various disciplines of chemistry.[3–7] If we very crudely sort the studies by objective, we can classically sort them either as improving on catalyst performance or on understanding the molecular processes happening during elementary reactions. Separating out individual influences or molecular mechanisms in a condensed-phase environment is challenging due to the high complexity of the catalyst material, many participating reactants and the reaction conditions.[7,8] This necessitates the design and use of model systems in well controlled environments to single out elementary reaction steps and investigate the properties of the catalyst as a function of the chosen conditions. One way to negate the influence of an environment is to not have one in the first place, that is to move the reaction into the gas phase. Small clusters present one possible model system for heterogeneous catalysts and have been explored since the early days of cluster chemistry.[9–14] To achieve better control over the composition of the cluster, ionic clusters are used, and by means of mass spectrometry the composition can be easily determined. Numerous techniques have been used to study the activation of methane by transition-metal clusters covering the periodic table.[3–5,15–20] It has been found that the elements of the 5d series are particularly reactive, down to the smallest possible model system: the mono-cation M^+.[15,21–25] While the ion, due its high charge density, is commonly more reactive than the corresponding condensed phase of the element, it allows us to concentrate on the intrinsic reactivity of the element towards methane. Hence, the mono-cation presents the ultimate single-site catalyst.[18]

The reaction of methane with the mono-cations of the 5d series is highly efficient and the thermal rates are close to, or on the order of, the collision

Open Access Article. Published on 20 May 2024. Downloaded on 5/21/2024 8:27:22 AM.
This article is licensed under a Creative Commons Attribution 3.0 Unported Licence.

rate.[15,21,22,26,27] At low collision energies, the main product channel is a species with the formal composition $[M,C,2H]^+$ and molecular hydrogen H_2. Thermodynamic arguments and recent spectroscopic investigations showed that the carbene $M{=}CH_2$ is the favoured isomer compared to the carbyne $H{-}M{-}CH^+$.[25] In the case of tantalum, the carbene structure has no C_{2v} symmetry but is slightly distorted due an agostic interaction between one of the hydrogen atoms and the tantalum cation.

$$Ta^+ + CH_4 \rightarrow TaCH_2^+ + H_2 \quad (1)$$

$$Ta^+ + CD_4 \rightarrow TaCD_2^+ + D_2 \quad (2)$$

Here, we present reactive scattering experiments using a crossed-beam 3D velocity map imaging set-up. This experimental technique allows us to gain insights into the energy- and angle-differential cross sections (DCS) of a reactive collision.[28–32] While the integral cross section, thermal reaction rate, structures of reaction products, and partly intermediates have been thoroughly investigated, direct experimental investigations into the dynamics of reactions (1) and (2) are missing. A reactive collision is an intrinsically dynamic process, and information on the dynamics of a reaction can be extracted from the DCS that is otherwise hidden or very hard to extract.[30–35] By interpreting the experimental velocity distributions with respect to the product ion speed and scattering angle, we can identify dynamic fingerprints. These encode information on the atomic-level rearrangement during the reaction, and on energy partitioning between the translational and internal degrees of freedom. Today, studies on the dynamics of ion molecule reactions by reactive scattering experiments are possible.[36–42] In the early 2000s, Weisshaar and co-workers investigated the reaction dynamics of transition-metal ions with hydrocarbon molecules using crossed-beam imaging. However, the experiment focused on cobalt and nickel cations in reactions with C_3–C_4-hydrocarbons.[43,44] The chemistry is dominated by the activation, that is cleavage, of the C–C bond and not the C–H bond. Early work by Armentrout and co-workers investigating integral cross sections of reactions between transition-metal ions and methane CH_4, molecular hydrogen H_2, and small hydrocarbon molecules with a C_2 backbone showed that the reactivity of methane much more resembles that of molecular hydrogen than that of the longer-chain hydrocarbon molecules.[12,45,46] A recent study by us revealed that the activation of carbon dioxide CO_2 by the tantalum cation is dominated by indirect dynamics despite the reaction rate being close to the collision rate[47] and the reaction being exothermic by more than 2 eV. We found a near constant kinetic energy release and that about 60% of the available energy is partitioned into internal degrees of freedom. We postulated that the reaction is trapped in the entrance well and that either the submerged barrier or the crossing point from the quintet to the triplet state is acting as an efficient bottleneck.[47] This shows again that experiments are important because chemical intuition and interpretations of stationary properties alone can be misleading[47,48] and underestimate the influences exerted by submerged barriers.[49] The mentioned multi-state reactivity is an accepted phenomenon in transition-metal chemistry.[50] If the reaction on the electronic ground state is associated with a high barrier, intersystem crossing (ISC) can occur and quite efficiently. ISC is, for example, assumed to happen with nearly

Open Access Article. Published on 20 May 2024. Downloaded on 5/21/2024 8:27:22 AM.
This article is licensed under a Creative Commons Attribution 3.0 Unported Licence.

unit probability for the heavy 5d elements. Similar to the reaction $Ta^+ + CO_2 \rightarrow TaO^+ + CO$, the reaction with methane forming the carbene is only possible at room temperature assuming ISC.[22] The efficiency of carbene formation in reaction (1) is similar to that of TaO^+ being formed in the oxygen atom transfer reaction. Reaction (1), however, is far less exothermic, and one might consider it even thermoneutral (see Fig. 1). Furthermore, the carbene formation is chemically much more evolved because it requires the cleavage of two C–H bonds and the subsequent formation of two new bonds and the release of molecular hydrogen from the tantalum ion. The mechanism resembles a classic two-step process of organometallic chemistry: (1) oxidative addition by insertion of the tantalum ion into a C–H bond followed by migration of a second H-atom to the metal centre and (2) reductive elimination of molecular hydrogen from the metal centre.[51–53]

Here, we present energy- and angle-differential cross sections as a function of collision energy for reaction (1), measured by velocity mapping the $TaCH_2^+$ product ion. The reaction is dominated by product ions isotropically scattered around the centre-of-mass, which is a fingerprint of indirect dynamics. However, we observe more anisotropy in the angular distributions than in the reaction with

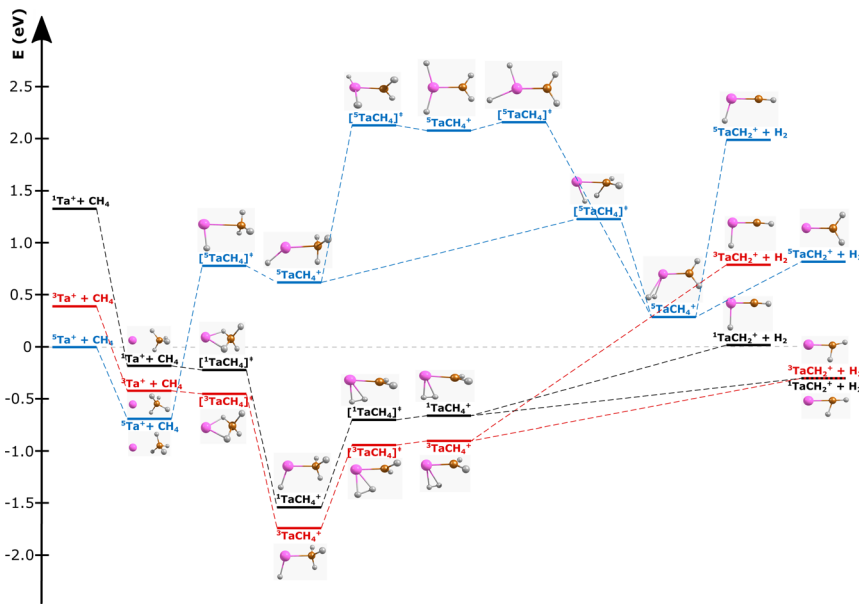

Fig. 1 Reaction pathway for $Ta^+ + CH_4 \rightarrow TaCH_2^+ + H_2$ with structures of the stationary points along the reaction coordinate (*i.e.*, for the pre-reaction complex (entrance channel), intermediates and post-reaction complexes, as well as the transition states) for the quintet surface (blue), triplet (red) and singlet (black). (Elements are denoted as follows: Ta = pink, carbon = orange, and hydrogen = white; structural data can be found in the ESI†). Energies are given in electron volts relative to the isolated ground-state reactants $^5Ta^+ + CH_4$. The given reaction energy of $E(^5Ta^+) = -0.3$ eV and energy splitting between $^5Ta^+$ and $^3Ta^+$ are used for calculating the kinematic cut-offs displayed in Fig. 2. Calculated at the CCSD(T)//B3LYP level (for details, see Methods). The energy of the transition states below the local minima is induced through the zero-point energy correction. The reaction pathway including transition states of lower importance is given in Fig. S1.†

Open Access Article. Published on 20 May 2024. Downloaded on 5/21/2024 8:27:22 AM.
This article is licensed under a Creative Commons Attribution 3.0 Unported Licence.

$Ta^+ + CO_2$, which hints at some more direct dynamics contributing. The velocity distributions and derived integrated angular and energy distributions are not as clear regarding their interpretation as for $Ta^+ + CO_2$, with some of the scattering signal found outside the energy range defined by the so-called kinematic cut-off. The experiments are complemented by *ab initio* calculations of the minimum energy path of reaction (1) for three spin multiplicities (quintet/triplet/singlet) of the tantalum cation Ta^+. We will first briefly introduce the experimental and theoretical methods used in the present study. The results section will begin with a discussion of the minimum energy pathway and is followed by the experimental results on the title reaction and a comparison to $Ta^+ + CD_4$. We will finish with a discussion of the recent results in comparison to the oxygen atom transfer reaction with CO_2 and conclude with an outlook on future experiments.

2 Methods

2.1 Experiment

In this experiment, we combine crossed beams with 3D velocity map imaging.[40,54,55] We generate an ion beam with a home-built laser vaporization source.[56,57] The second harmonic of an Nd:YAG laser (532 nm, 20 Hz, $\approx$ 4 mJ per pulse (5×10^7 W cm^{-2})) is focused on a rotating tantalum target. The ions in the produced plasma are extracted by a synchronized transverse helium pulse (8 bar of helium, 40 μs) into the interaction region of the source. The ion beam passes through an expansion channel (61 mm length, 2 mm diameter) where the ions undergo about 10^4 collisions with helium before expanding into the high vacuum (approx. 5×10^{-6} mbar in operation).[47] So far, we have no direct control over the electronic states of the produced tantalum cations. However, it is assumed that no significant amounts of electronically excited tantalum cations are produced, as the formation of electronically excited tantalum cations is not only energetically demanding, but also statistically disadvantaged.[2,47] The conditions of the ion source are adjusted in such a way that tantalum cations are generated and the formation of ionic tantalum clusters is suppressed at the same time. The ion beam passes through an aperture before it is focused by several Einzel lenses and deflectors, and finally transferred to the interaction region of the velocity map imaging spectrometer. In this process, the energy of the ion beam and to some degree its angle can be adjusted. The ion beam is characterised by velocity mapping. In the interaction zone, the ion beam is crossed with a neutral beam generated using a home-built piezo valve.[58] Pure CH_4 is expanded and enters the interaction zone through a skimmer. The molecular beam can be characterized in a similar way to the ion beam; the ionization of the neutral beam takes place by non-resonant electron impact ionization. The two beams are crossed at an angle of $\approx$150° and the resulting product ions are then accelerated perpendicularly in the direction of the time- and position-sensitive detector unit. The detector unit consists of a combination of microchannel plates and a phosphor screen with a camera to record the position of ion impact, as well as a photo multiplier tube to record the time of arrival. All three velocity components can then be extracted from the measured data sets in such a way that the Newton sphere can finally be reconstructed.[54] The analysis of the recorded data is based on an established routine from Wester and co-workers.[40,54,59] The recovered 3D Newton spheres are visualized in 2D representations, where the velocity distributions of the product

Open Access Article. Published on 20 May 2024. Downloaded on 5/21/2024 8:27:22 AM.
This article is licensed under a Creative Commons Attribution 3.0 Unported Licence.

ions are represented as 2D histograms using the velocity component v_x and the radial velocity v_r (which is obtained from the velocity components v_z and v_y). An integration of the original distributions over the solid angle or the energy gives the 1D histograms, which are normalized to the unit area if not stated otherwise.

2.2 Theory

Minima and transition states along the $Ta^+ + CH_4$ reaction pathway were optimized employing density functional theory (DFT) with the B3LYP functional and the aug-cc-pVTZ basis set on C and H, and the ECP60MDF_AVTZ basis set on Ta.[60] To obtain more accurate electronic energies, single-point recalculation at the coupled cluster level, CCSD(T), with the same basis set was performed, employing the zero-point energy correction as obtained at the DFT level. This approach was shown to work reasonably well for the $[TaCO_2]^+$ system.[47] Further benchmarking is provided in the ESI,† including comparison to multi-reference calculations and a comparison of Ta–H. Armentrout and co-workers also did benchmarking for reactants and/or products participating in the present reaction.[22,61] To make sure that the lowest-lying solution of the electronic Schrödinger equation was obtained in the given spin multiplicity, wave-function stabilization was performed prior to every single-reference calculation. Single-reference calculations were performed in the Gaussian quantum chemical program,[62] and multi-reference ones in Molpro.[63–65]

3 Results and discussion

The carbene $TaCH_2^+$ formation is the dominant reaction pathway for methane with 5d transition-metal cations. A conceivable reaction all the way to the carbide TaC^+ is endothermic by more than 3 eV. Three spin states have been considered by us for reaction (1): quintet, triplet and singlet. The respective structures and energies of the stationary points are shown in Fig. 1. If we look at the product ion $TaCH_2^+$, the energies of the triplet and singlet states are indistinguishable from each other. The whole reaction pathways for the triplet (red trace) and singlet (black trace) states go in parallel, while the quintet (blue trace) follows a somewhat different pathway. The reaction of $^5Ta^+$ with methane is associated with a barrier of almost 1.5 eV, whereas starting from the triplet state $^3Ta^+$ (or singlet state $^1Ta^+$), the reaction shows all the features common to an exothermic gas phase ion molecule reaction with all transition states submerged relative to the free reactants. Intersystem crossing (ISC) has to occur before the first transition state on the quintet surface for the reaction to efficiently happen at room temperature (Fig. 1). The crossing is only reasonably possible in the vicinity of the first triplet transition state, which is related to the formation of the first hydrogen–tantalum bond. Crossing to the singlet surface is possible but unlikely because it lies higher in energy and can be assumed to have a lower crossing probability compared to crossing to the triplet surface because two spin flips are required. The crossing to the triplet surface is the commonly assumed pathway and $^3[HTaCH_3]^+$ is formed as an intermediate.[22,66–68] Subsequently, a second hydrogen atom moves to the tantalum atom which leads to $[H_2TaCH_2]^+$, from which molecular hydrogen is eliminated. Two isomers are possible for the $[Ta,C,2H]^+$ product but the carbene $[TaCH_2]^+$ is the lower energy isomer compared

 This journal is © The Royal Society of Chemistry 2024

Open Access Article. Published on 20 May 2024. Downloaded on 5/21/2024 8:27:22 AM.
This article is licensed under a Creative Commons Attribution 3.0 Unported Licence.

to the carbyne $[HTaCH]^+$. Preferential carbene formation for $[TaCH_2]^+$ has also been spectroscopically confirmed.[25]

Here, we present angle- and energy-differential cross sections for the title reaction (reaction (1)) from which we can gain insight into the dynamics of the carbene formation. We studied the reaction as a function of relative collision energy (0.7 eV, 1.1 eV and 1.3 eV). The product ion velocity distributions together with the integrated angular distributions are given in Fig. 2.

At the lowest investigated relative collision energy, we observe an isotropic distribution of the $TaCH_2^+$ around the center-of-mass (Fig. 2a). This velocity distribution is a common signature for indirect dynamics.[29] In this atomistic mechanism, the reactants form a long-lived complex, whose lifetime outlasts several rotational periods. The complex subsequently decays statistically in all spatial directions. During the complex's lifetime, kinetic energy can be efficiently redistributed into rotational and vibrational modes of molecular products, here $TaCH_2^+$ and H_2. This specific symmetric signature has already been observed in other ion-molecule reactions[36,47,69,70] and is usually associated with small impact parameter collisions and efficient transfer of angular momentum of the collision into rotational angular momentum of molecular products.[29–31] The isotropic scattering becomes even more obvious in the integrated angular distribution,

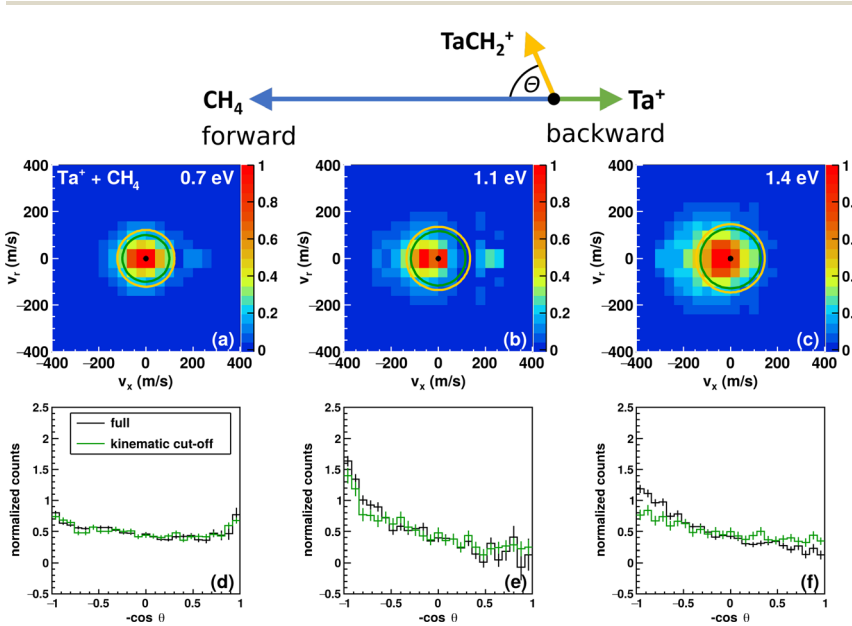

Fig. 2 Experimental differential cross sections. The velocity distributions of $TaCH_2^+$ at three different relative collision energies (0.7 eV, 1.1 eV and 1.3 eV) are shown in the top row (a–c). The superimposed circles show the kinematic cut-off for the reaction between $^5Ta^+$ and methane (green), and $^3Ta^+$ and methane (orange). The bottom row (d–f) shows the corresponding angular distributions for the respective collision energies (black line). The green histogram shows the angular distribution of the events within the kinematic cut-off assuming $^5Ta^+$, that is the events within the green circle. The simplified Newton diagram at the top indicates the relative orientations of the reactant beams and the $TaCH_2^+$ scattering direction in the center-of-mass frame.

Open Access Article. Published on 20 May 2024. Downloaded on 5/21/2024 8:27:22 AM.
This article is licensed under a Creative Commons Attribution 3.0 Unported Licence.

which shows a constant scattering probability for the whole scattering range (see black trace in Fig. 2d). It is apparent that events can be found outside the velocity space defined by the kinematic cut-off. The kinematic cut-offs are depicted by the green and orange rings superimposed onto the scattering distributions and give the maximum possible product kinetic energy taking energy and momentum conservation into account given that the experiments are conducted under single-collision conditions. The available energy is defined by the relative collision energy E_{rel}, (possible) internal energy of the reactants and the energy freed or consumed by the reaction, which we refer to as reaction exothermicity E_{exo}. Here, we use the reaction exothermicity as shown in Fig. 1. Experimental uncertainties for the product ion velocities (and energies) are derived by Gaussian error propagation based on the energy and angular spread of the reactant beams.[54] A graphical representation of the errors superimposed onto the velocity distributions at the kinematic cut-off is shown in Fig. S5.† If the relative collision energy is increased, some changes in the reaction dynamics can be observed. An asymmetry in the velocity distribution of the product ions emerges. It is also obvious that an even greater fraction of events can be found outside the kinematic cut-off. At 1.3 eV relative collision energy, the majority of events are scattered within the forward hemisphere, that is the initial direction of the neutral beam. An asymmetric velocity distribution is a sign of a direct atomistic mechanism. Taking the kinematics into account, namely a much heavier ion ($m(Ta^+) = 181$ amu) compared to the neutral reactant ($m(CH_4) = 16$ amu), scattering of $TaCH_2^+$ into the forward hemisphere means that the tantalum ion turns around. We observe what is generally termed as direct rebound. However, the majority of events are still scattered isotropically, especially within the kinematic-cut off (see green histograms in Fig. 2d–f).

The integrated kinetic energy distributions do not significantly differ from each other as function of relative collision energy (see Fig. 3 and S3†). The distributions just broaden with increasing collision energy. As discussed above, the absolute kinetic energy of the product ion $TaCH_2^+$ is very small due to the high mass difference of both products ($m(TaCH_2^+) = 195$ amu and $m(H_2) = 2$ amu) and the required momentum conservation. The corresponding internal energy E_{int} distributions are given in Fig. S2 and S3.† The distributions slightly shift towards larger values with increasing collision energy indicating that at least part of the additional collision energy is partitioned into ro-vibrational excitation of either $TaCH_2^+$ or H_2. Due to the experimental uncertainty, we will not discuss the energy partitioning in more detail.

$$E_{rel} + E_{exo} = E_{kin}(TaCH_2^+) + E_{kin}(H_2) + E_{int} \quad (3)$$

The trend in the velocity distribution towards the forward hemisphere for $TaCH_2^+$ in the reaction with methane (reaction (1)) was not expected by us. To further exclude systematic errors, we therefore decided to carry out the reaction at the highest investigated relative collision energy with fully deuterated methane CD_4 (Fig. 4). This sounds trivial but gives us a product ion $TaCD_2^+$ with a mass-to-charge ratio m/z of 197, which makes gating our detector with respect to the time-of-flight trace a little less challenging (see Table S1†). Fig. 4 shows the differential cross section for reactions (1) and (2) at a comparable relative collision energy.

 This journal is © The Royal Society of Chemistry 2024

Open Access Article. Published on 20 May 2024. Downloaded on 5/21/2024 8:27:22 AM.
This article is licensed under a Creative Commons Attribution 3.0 Unported Licence.

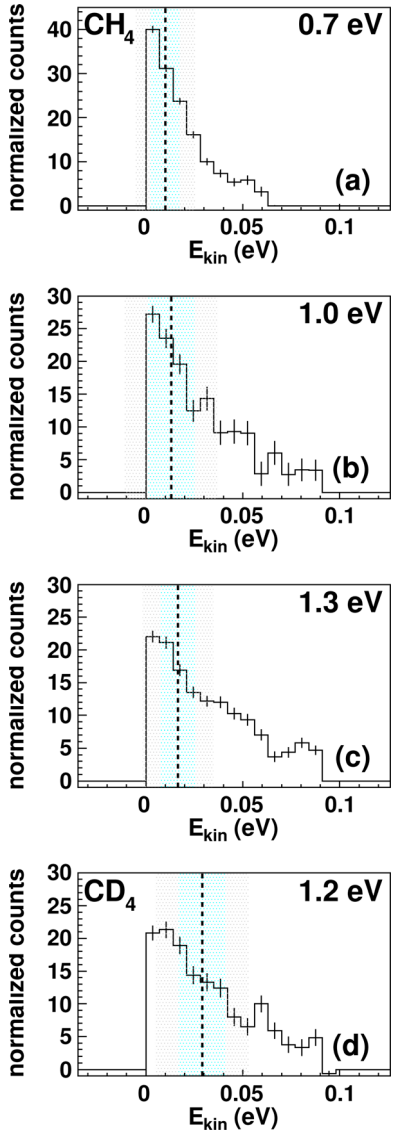

Fig. 3 Kinetic energy E_{kin} distributions for $TaCH_2^+$ (a–c) and $TaCD_2^+$ (d). The energy resolution is calculated using Gaussian error propagation from the energy and angular spread of the reactant beams.[54] The $\pm 1\sigma$-error interval is given by the light blue area and the $\pm 2\sigma$-error interval by the grey one. The distributions extend beyond the kinematic cut-offs given by energy and momentum conservation with respect to the relative collision energy E_{rel} and the reaction exothermicity E_{exo}. In other words, this means that an unavailable amount of energy is converted into kinetic energy.[71] Possible explanations are missing contributions to the energy balance, for example, electronically excited states of Ta^+ contributing or the internal energy of CH_4. The relative contributions of events scattered within the kinematic cut-off and the two shown error-intervals are given in Table 1.

Open Access Article. Published on 20 May 2024. Downloaded on 5/21/2024 8:27:22 AM.
This article is licensed under a Creative Commons Attribution 3.0 Unported Licence.

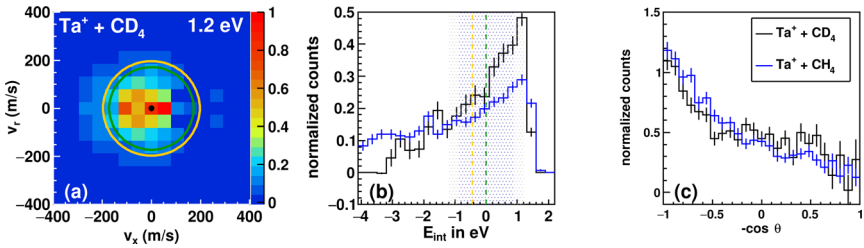

Fig. 4 Differential cross section of the reaction between $Ta^+ + CD_4$ at 1.2 eV (a). Kinematic cut-offs (green: $^5Ta^+$; orange: $^3Ta^+$ are superimposed and calculated using the exothermicities given in Fig. 1. (b) Integrated internal energy distributions for the reaction with CD_4 in black and CH_4 in blue together with the $\pm1\sigma$-error illustrated as a shaded area around the kinematic cut-off of the ground-state reaction (CD_4 in blue and CH_4 in grey), which is given as the vertical line (green). The $\pm1\sigma$-error is derived from Gaussian error propagation of the energy and angular spread of the reactant beams.[54] (c) The integrated angular distribution for the reaction with CD_4 in black and CH_4 in blue.

Similar scattering signatures are observed for $TaCH_2^+$ and $TaCD_2^+$. This suggests that both reactions proceed by a very similar mechanism. This is in line with our expectations, since the dominant scattering signature is indirect and therefore most likely statistical regarding the energy partitioning. In addition, the chemical properties of the reactants do not significantly change upon going from CH_4 to CD_4.

The integrated angular distributions for reactions with CH_4 and CD_4 (Fig. 4c) confirm the impression from the velocity distributions. The distribution of the internal energy E_{int} in the reaction with CD_4 is very similar to the one in the reaction with CH_4 and seems to be slightly narrower, *i.e.*, with less events outside the kinematic cut-off (see Table 1). The general forms of the distribution for both reactions hardly differ from each other. Minor deviations can of course be due to differences in kinematics, but also to isotope effects. However, the experiments with d4-methane confirm the observations made with methane. The kinematic cut-off for reaction (2) is calculated using the reaction exothermicity for $Ta^+ + CH_4$ corrected for the zero-point energy contribution of $\approx$+0.10 eV.

Table 1 The table lists the 1σ-error to the product ion velocity at the kinematic cut-off for $Ta^+ + CH_4 \rightarrow TaCH_2^+ + H_2$. In addition, the fraction f of the events within the kinematic cut-off (f_{kc}) is given. This is extended by increasing the kinematic cut-off by 1σ ($f_{kc+1\sigma}$) and 2σ ($f_{kc+2\sigma}$). The whole scattering range of $\theta = 0$–180° has been evaluated. Omitting the scattering range from $\theta = 160$–180° leads only to minor variations

	Relative collision energy (eV)			
	0.7	1.0	1.3	1.2 (CD_4)
$v_{kc}(TaCH_2^+)$ (m s^{-1})	102	115	128	169
1σ-error $v_{kc}(TaCH_2^+)$ (m s^{-1})	37	52	35	72
f_{kc}/%	33	36	39	54
$f_{kc+1\sigma}$/%	58	50	61	84
$f_{kc+2\sigma}$/%	81	66	81	$\approx$100

 This journal is © The Royal Society of Chemistry 2024

Open Access Article. Published on 20 May 2024. Downloaded on 5/21/2024 8:27:22 AM.
This article is licensed under a Creative Commons Attribution 3.0 Unported Licence.

We observed a large amount of events scattered outside the kinematic cut-off. We discuss these events below, including why a majority of these events can be explained by the experimental uncertainties. The fraction of events scattered with the kinematic cut-off and the $\pm 1\sigma$ and $\pm 2\sigma$-interval defined by the error of the product ion velocity are presented in Table 1. The fractions for the respective intervals are on the order of what to theoretically expect. Comparing the error to the product ion velocity in absolute numbers for the reactions with H_2 and D_2 at comparable relative collision energies, we see that although the error is on the same order, the fraction of events found within the kinematic cut-off is significantly higher in the case of CD_4. The present reactions suffer from unfortunate kinematics, *i.e.*, a high mass difference between the two product species. A similar observation of a significant number of events scattered outside the $\pm 2\sigma$-interval has been seen before in ion-molecule reactive scattering experiments.[71] Additionally, the tantalum ion is very heavy compared to the neutral reactant, and the uncertainties of the reactant ion beam are larger than the ones of the molecular beam of the neutral reactants. Thus, a careful adjustment and monitoring of the ion-beam performance is required. An example of this effect is given in the ESI (Fig. S4).†

Events found outside the expected scattering range could also be due to a missing contribution to the energy balance (eqn (3)), which puts the kinematic cut-off at the wrong value. The presence of electronically excited states of Ta^+ seems to be the most obvious source of additional energy for the present reaction. The first electronically excited state is a triplet about 0.4 eV above the ground state.[2] The kinematic-cut off for this potential reactant state is indicated by the orange circles in Fig. 2a–c. We do not assume contributions from this state to be a significant source for the high velocity events found. Firstly, as can be seen, the velocity spacing between the kinematic cut-offs is small (≈ 20 m s^{-1}). Secondly, in a previous study, we gave an upper limit of about 20% contribution of the first electronically excited triplet. Here, we used similar source conditions (He backing pressure, laser power, timings) as for recording the $Ta^+ + CO_2$ data[47] and we recorded the data with a break in between measurements and two different piezo valves in the ion source and observed similar signatures in the velocity distributions. We should also keep in mind that the spin–orbit manifold of the quintet spans 0.8 eV and significantly overlaps with the manifold of the first triplet state. Another contribution to the energy balance could be internal excitation of the methane. However, we consider methane to have little or no vibrational excitation given our source conditions and for it to be rotationally cold.

Besides the arguments related to the energy balance, a different product channel could be the source of events found outside the expected range. A different center-of-mass combined with a different exothermicity leads to scattering observed in a different area. To account for the observed events, we would need (a) a more favourable mass ratio of the two products and (b) an exothermic reaction. For the reaction $Ta^+ + CH_4/CD_4$, the carbene formation is the lowest energy channel, and up to 2 eV relative collision energy no other product channels were observed in guided ion beam experiments.[22] The first product to appear is TaH^+, which we would not have been able to detect due to the mass difference of 1 amu. The conceivable formation of the carbide TaC^+ is beyond the energy range of the present experiment because TaC^+ formation is endothermic by more than 3.2 eV. We do not see any evidence in the time-of-flight trace for higher-mass

Open Access Article. Published on 20 May 2024. Downloaded on 5/21/2024 8:27:22 AM.
This article is licensed under a Creative Commons Attribution 3.0 Unported Licence.

products. We, therefore, conclude that we do not have a second product channel contributing. Another possibility to consider is that we do have a different reactant ion or neutral reactant present. We expand a pure CH_4 beam with the CH_4 used from the gas cylinder. The carbene formation is highly efficient, *i.e.*, on the order of 10% of the collision rate. Any contamination would have to be present in the interaction region at the timing of the crossing of the two beams, at a density plus cross section to compete with methane. This is highly unlikely and we exclude this possibility. We saw no evidence of cluster formation in the expansion. A contamination to the ion beam at the levels needed is also unlikely. The small time-of-flight differences between the reactant and product ion makes us sensitive to contamination (see Table S1† for TOF-values). The ion beam is orders of magnitudes more intense than the product ion signal. We set the amplification for scattering experiments to single-ion counting mode. The most likely 'contaminations' from the source are TaO^+ and TaC^+. If we have any traces of these present, and so far we only saw TaO^+, we cannot run a scattering experiment. The TaO^+ could always be traced back to leaks in the gas lines after maintenance of the source. The stability of the ion beam is key for our reactive scattering experiments. We expect that the addition of an ion trap into the ion beam path will help with the long-term stability of the ion beam.

3.1 Comparison to $Ta^+ + CO_2$

This study investigated the reaction between tantalum cations and methane at three different relative collision energies up to approximately 1.3 eV. Initially, an isotropic distribution around the center-of-mass is observed, which gains some forward contribution as the relative collision energy increases. At low relative collision energy, we observe scattering signatures that are very similar to the experimental velocity distributions for the reaction between tantalum cations and carbon dioxide (reaction (4)).[47] For the oxygen atom transfer, a slight asymmetry towards the forward hemisphere in the velocity distribution of the TaO^+ was observed only at 2.0 eV collision energy. This trend is more obvious for the reaction with methane, with an onset at much lower collision energies. At this point, it is interesting to discuss the chemical and physical differences between carbon dioxide and methane.

$$Ta^+ + CO_2 \rightarrow TaO^+ + CO \quad (4)$$

It is obvious that only four atoms are involved in the reaction with CO_2, whereas six atoms are involved in the reaction with methane. Reaction (1) is much more complex and will be a major challenge for theory, especially for quantum theory. In both reactions (reactions (1) and (4)), diatomic neutral products are formed and a double bond to the tantalum cation is formed. At first glance this indicates a similarity, but the chemistry of both reactions is very different. The long-range interaction between Ta^+ and CO_2 is dominated by the charge-quadrupole term and steers the reactants into a co-linear pre-reaction complex.[47,72] During the reaction, the geometry shifts over to a bent configuration, potentially allowing for torque between TaO^+ and CO to occur. The data of Meta *et al.* shows that most of the available energy is transferred into internal degrees of freedom of the products, which means into vibrational and rotational modes of TaO^+ and/or CO.[47] Reaction (1) is chemically much more complicated.

 This journal is © The Royal Society of Chemistry 2024

Open Access Article. Published on 20 May 2024. Downloaded on 5/21/2024 8:27:22 AM.
This article is licensed under a Creative Commons Attribution 3.0 Unported Licence.

The bond between the two hydrogen atoms to the carbon atom must first be broken while Ta–H bonds are formed. These are cleaved when the H–H bond is formed to release molecular hydrogen H_2. The experimental data also indicate that the available energy is not exclusively transferred into internal energy, but that a substantial part goes into the kinetic energies of the reaction products, although we have to tread carefully here. We now want to speculate on why the more complex and less exothermic chemical transformation seems to slightly favour direct dynamics. The central carbon atom in CH_4 is partially negatively charged due to its slightly higher electronegativity relative to hydrogen. This is a difference compared to CO_2, for which the negative charge is more centred on oxygen atoms. In contrast to CO_2, methane also has no appreciable quadrupole moment, which makes the charge-induced dipole interaction the leading term for the long-range potential. The well depth of the pre-reaction complex $[TaCH_4]^+$ is similar to that of $[TaCO_2]^+$, but the barrier to the first transition state (^{3}TS) is lower in the case of $Ta^+ + CH_4$ and associated with less structural rearrangement. This might result in a better coupling of translation to the reaction coordinate compared to reaction (4). Even though more atoms are involved and more bonds are cleaved, formed and rearranged, the overall geometry changes at the carbon atom appear not as pronounced for $Ta^+ + CH_4$ as for $Ta^+ + CO_2$ when crossing over the first transition state. The crossing is followed by a second H-abstraction, which needs about 1 eV for the intermediate $[HTaCH_3]^+$ to transfer a second hydrogen atom to the tantalum and is followed by H_2 formation. Once the second H-atom is abstracted, the surface is rather flat and not associated with another barrier that could act as a bottle-neck. All of the above arguments are speculative and could be answered by trajectory simulations that are not available yet.

4 Conclusions

We presented energy- and angle-differential cross sections for the reaction $Ta^+ + CH_4 \rightarrow TaCH_2^+ + H_2$ as a function of collision energy. The dynamics of the reaction are dominated by an indirect complex-mediated mechanism that allows for efficient partitioning of energy into internal degrees of freedom. The present reaction shows a little more direct character compared to the oxygen atom transfer reaction $Ta^+ + CO_2 \rightarrow TaO^+ + CO$. For both systems, the direct mechanism leads to scattering into the forward hemisphere due to a direct rebound, that is turn-around of the tantalum indicative of a head-on collision. The experimental velocity distributions extend beyond the kinematic cut-off defined by the energy balance of the collision: relative collision energy, internal energy of Ta^+ and CH_4, and reaction exothermicity. The majority of events found outside the kinematic cut-off fall into the $\pm 2\sigma$-interval defined by the uncertainty of the product ion velocity distribution. If we are missing contributions to the energy balance, from which we derive the kinematic cut-off, the most obvious missing candidates are (1) an electronically excited state of Ta^+ or (2) calculations not being converged despite the high level employed here. We will further address these open questions by investigating another transition metal, having a more detailed look into the source conditions, and by further testing different levels of theory. The theoretical description of open-shell transition-metal species is notoriously difficult due to the strong multi-reference character and thus we need further collaborations between experiment and theory. A final answer might be

Open Access Article. Published on 20 May 2024. Downloaded on 5/21/2024 8:27:22 AM.
This article is licensed under a Creative Commons Attribution 3.0 Unported Licence.

given by comparison with trajectory simulations. The present data set will be subject to further scrutiny from ourselves, for example, by repeating experiments at lower collision energy with CD_4 once the ion trap is built in. The design follows that of the imaging experiment developed by the Wester group.[69] While we do not expect the intrinsic velocity spread of the ion beam to reduce significantly below the current values for individual measurements, we expect a better long-term stability in the central velocity of the beam and the angular spread. These two points lead to an uncertainty in the centre-of-mass of the collision, which is known to generally be the main error in reactive ion molecule scattering.

The carbene $TaCH_2^+$ presents a reactive carbon centre that can readily undergo further reactions. For example, it is known that platinum or iridium cations can undergo reactions with more than one methane molecule.[24,73–75] In the next step, we will modify our crossed-beam imaging experiment by including a radio-frequency ion trap into the ion beam path, similar to the instrument operated by the Wester group.[54,76] Reactive carbon species will be formed *in situ* in the ion trap[77] and transferred into the interaction region of the velocity map imaging spectrometer. We aim for $[M–CH_3]^+$ and $[MCH_2]^+$ carbon species to investigate whether C–C coupling reactions occur with small hydrocarbons such as methane or ethylene. These reactions are postulated to proceed *via* cyclic transition states, but if they occur *via* a step-wise or concerted mechanism is still debated. Our aim is to contribute to this debate by exploring the dynamics of C–C coupling reactions.

Author contributions

M. M., M. E. H., M. B. and M. W. carried out the crossed-beam experiments and analysed the data; M. O. performed and analyzed the quantum chemical calculations; J. M. supervised and devised the experiment; M. M., M. O. and J. M. prepared the manuscript, J. M. and M. O. coordinated the study.

Conflicts of interest

There are no conflicts to declare.

Acknowledgements

J. M. thanks the Deutsche Forschungsgemeinschaft DFG (Project number 500279291) for support of this project. M. M. acknowledges support by the DFG through the SFB TRR88/3MET. The computational results presented have been achieved using the HPC infrastructure LEO of the University of Innsbruck. M. M., M. B., M. W. and J. M. acknowledge and thank Roland Wester and Björn Bastian for providing the data analysis software package for the reactive scattering data. We thank Roland Wester, Nicholas S. Shuman and Shaun G. Ard for valuable discussions of the presented results. We thank Roland Wester, Nicholas S. Shuman, Shaun G. Ard and Hua Guo for valuable discussions of the presented results.

Notes and references

1 D. R. Lide, *CRC Handbook of Chemistry and Physics*, CRC Press, 84th edn, 2003.

 This journal is © The Royal Society of Chemistry 2024

Open Access Article. Published on 20 May 2024. Downloaded on 5/21/2024 8:27:22 AM.
This article is licensed under a Creative Commons Attribution 3.0 Unported Licence.

2 ed. A. Kramida, Y. Ralchenko, J. Reader, and N. I. S. T. A. S. D Team, **http://physics.nist.gov/asd/**.
3 H. Schwarz, *Angew. Chem., Int. Ed.*, 2011, **50**, 10096–10115.
4 J. Roithová and D. Schröder, *Chem. Rev.*, 2010, **110**, 1170–1211.
5 J. Roithová and J. M. Bakker, *Mass Spectrom. Rev.*, 2022, **41**, 513–528.
6 A. Hu, J.-J. Guo, H. Pan and Z. Zuo, *Science*, 2018, **361**, 668.
7 M. Ravi, M. Ranocchiari and J. A. van Bokhoven, *Angew. Chem., Int. Ed.*, 2017, **56**, 16464–16483.
8 H. Arakawa, M. Aresta, J. N. Armor, M. A. Barteau, E. J. Beckman, A. T. Bell, J. E. Bercaw, C. Creutz, E. Dinjus, D. A. Dixon, K. Domen, D. L. DuBois, J. Eckert, E. Fujita, D. H. Gibson, W. A. Goddard, D. W. Goodman, J. Keller, G. J. Kubas, H. H. Kung, J. E. Lyons, L. E. Manzer, T. J. Marks, K. Morokuma, K. M. Nicholas, R. Periana, L. Que, J. Rostrup-Nielson, W. M. H. Sachtler, L. D. Schmidt, A. Sen, G. A. Somorjai, P. C. Stair, B. R. Stults and W. Tumas, *Chem. Rev.*, 2001, **101**, 953–996.
9 K. K. Irikura and J. L. Beauchamp, *J. Am. Chem. Soc.*, 1991, **113**, 2769–2770.
10 M. M. Kappes and R. H. Staley, *J. Phys. Chem.*, 1981, **85**, 942–944.
11 M. M. Kappes and R. H. Staley, *J. Am. Chem. Soc.*, 1981, **103**, 1286–1287.
12 P. B. Armentrout and J. L. Beauchamp, *Acc. Chem. Res.*, 1989, **22**, 315–321.
13 G. Albert, C. Berg, M. Beyer, U. Achatz, S. Joos, G. Niedner-Schatteburg and V. E. Bondybey, *Chem. Phys. Lett.*, 1997, **268**, 235–241.
14 J. C. Weisshaar, *Acc. Chem. Res.*, 1993, **26**, 213–219.
15 P. B. Armentrout, *Mass Spectrom. Rev.*, 2022, **41**, 606–626.
16 H. Schwarz, *Isr. J. Chem.*, 2014, **54**, 1413–1431.
17 A. Fielicke, *Chem. Soc. Rev.*, 2023, **52**, 3778–3841.
18 D. K. Bohme and H. Schwarz, *Angew. Chem., Int. Ed.*, 2005, **44**, 2336–2354.
19 S. M. Lang and T. M. Bernhardt, *Phys. Chem. Chem. Phys.*, 2012, **14**, 9255–9269.
20 K. R. Asmis and A. Fielicke, *Top. Catal.*, 2018, **61**, 1–2.
21 A. Shayesteh, V. V. Lavrov, G. K. Koyanagi and D. K. Bohme, *J. Phys. Chem. A*, 2009, **113**, 5602–5611.
22 L. G. Parke, C. S. Hinton and P. B. Armentrout, *J. Phys. Chem. C*, 2007, **111**, 17773–17787.
23 R. Wesendrup and H. Schwarz, *Angew. Chem., Int. Ed.*, 1995, **34**, 2033–2035.
24 O. W. Wheeler, M. Salem, A. Gao, J. M. Bakker and P. B. Armentrout, *J. Phys. Chem. A*, 2016, **120**, 6216–6227.
25 V. J. F. Lapoutre, B. Redlich, A. F. G. van der Meer, J. Oomens, J. M. Bakker, A. Sweeney, A. Mookherjee and P. B. Armentrout, *J. Phys. Chem. A*, 2013, **117**, 4115–4126.
26 J. Lengyel, N. Levin, M. Ončák, K. Jakob, M. Tschurl and U. Heiz, *Chem. - Eur. J.*, 2022, **29**, e202203259.
27 J. F. Eckhard, T. Masubuchi, M. Tschurl, R. N. Barnett, U. Landman and U. Heiz, *J. Phys. Chem. A*, 2021, **125**, 5289–5302.
28 Y. Lee, *Science*, 1987, **236**, 793.
29 D. R. Herschbach, *Angew. Chem., Int. Ed.*, 1987, **26**, 1221–1243.
30 R. D. Levine, *Molecular Reaction Dynamics*, Cambridge University Press, 2009.
31 *Tutorials in Molecular Reaction Dynamics*, ed. M. Brouard and C. Vallance, RSC Publishing, 2012.
32 X. Yang, D. C. Clary and D. M. Neumark, *Chem. Soc. Rev.*, 2017, **46**, 7481–7482.
33 P. Casavecchia, *Rep. Prog. Phys.*, 2000, **63**, 355.

Open Access Article. Published on 20 May 2024. Downloaded on 5/21/2024 8:27:22 AM.
This article is licensed under a Creative Commons Attribution 3.0 Unported Licence.

34 K. Liu, *Annu. Rev. Phys. Chem.*, 2016, **67**, 91–111.
35 E. Carrascosa, J. Meyer and R. Wester, *Chem. Soc. Rev.*, 2017, **46**, 7498–7516.
36 J. Mikosch, S. Trippel, C. Eichhorn, R. Otto, U. Lourderaj, J. X. Zhang, W. L. Hase, M. Weidemueller and R. Wester, *Science*, 2008, **319**, 183–186.
37 J. Meyer and R. Wester, *Annu. Rev. Phys. Chem.*, 2017, **68**, 333–353.
38 L. Pei, E. Carrascosa, N. Yang, S. Falcinelli and J. M. Farrar, *J. Phys. Chem. Lett.*, 2015, **6**, 1684–1689.
39 M.-M. He, J. Hu, C.-X. Wu, Y. Zhi and S. X. Tian, *J. Phys. Chem. A*, 2020, **124**, 3358–3363.
40 J. Meyer, V. Tajti, E. Carrascosa, T. Győri, M. Stei, T. Michaelsen, B. Bastian, G. Czakó and R. Wester, *Nat. Chem.*, 2021, **13**, 977–981.
41 G. Zhang, D. Lu, Y. Ding, L. Guan, S. Han, H. Guo and H. Gao, *Nat. Chem.*, 2023, **15**, 1255–1261.
42 D. Swaraj, T. Michaelsen, A. Khan, F. Zappa, R. Wild and R. Wester, *Mol. Phys.*, 2024, **122**, e2194455.
43 E. L. Reichert and J. C. Weisshaar, *J. Phys. Chem. A*, 2002, **106**, 5563–5576.
44 S. S. Yi, E. L. Reichert, M. C. Holthausen, W. Koch and J. C. Weisshaar, *Chem.–Eur. J.*, 2000, **6**, 2232–2245.
45 P. B. Armentrout, *Science*, 1991, **251**, 175–179.
46 D. Schroeder, H. Schwarz, D. E. Clemmer, Y. Chen, P. B. Armentrout, V. I. Baranov and D. K. Boehme, *Int. J. Mass Spectrom. Ion Processes*, 1997, **161**, 175–191.
47 M. Meta, M. E. Huber, T. Michaelsen, A. Ayasli, M. Ončák, R. Wester and J. Meyer, *J. Phys. Chem. Lett.*, 2023, **14**, 5524–5530.
48 M. Stei, E. Carrascosa, M. A. Kainz, A. H. Kelkar, J. Meyer, I. Szabó, G. Czakó and R. Wester, *Nat. Chem.*, 2016, **8**, 151–156.
49 H. Song and H. Guo, *ACS Phys. Chem. Au*, 2023, **3**, 406–418.
50 D. Schroeder, S. Shaik and H. Schwarz, *Acc. Chem. Res.*, 2000, **33**, 139–145.
51 C. Elschenbroich, *Orgonametallchemie*, Springer Vieweg, 6th edn, 2008.
52 F. Breher, in *Organometallverbindungen*, ed. R. L. K. James, E. Huheey and E. A. Keiter, deGruyter, 2014, ch. 15, pp. 757–939.
53 M. Lersch and M. Tilset, *Chem. Rev.*, 2005, **105**, 2471–2526.
54 R. Wester, *Phys. Chem. Chem. Phys.*, 2014, **16**, 396–405.
55 A. T. J. B. Eppink and D. H. Parker, *Rev. Sci. Instrum.*, 1997, **68**, 3477–3484.
56 D. Proch and T. Trickl, *Rev. Sci. Instrum.*, 1989, **60**, 713–716.
57 V. E. Bondybey and J. H. English, *J. Chem. Phys.*, 1981, **74**, 6978–6979.
58 D. Gerlich, G. Jerke, U. Mueck and U. Person, *Schnelles Ventil zur Erzeugung sehr kurzer Gasimpulse, Internal Document Physics Department*, Freiburg University, Germany, 1990, **http://www.tu-chemnitz.de/physik/ION/Technology**.
59 S. Trippel, M. Stei, R. Otto, P. Hlavenka, J. Mikosch, C. Eichhorn, A. Lourderaj, J. Zhang, W. L. Hase, M. Weidemüller and R. Wester, *J. Phys.: Conf. Ser.*, 2009, **194**, 012046.
60 D. Figgen, K. A. Peterson, M. Dolg and H. Stoll, *J. Chem. Phys.*, 2009, **130**, 164108.
61 C. S. Hinton, F. Li and P. Armentrout, *Int. J. Mass Spectrom.*, 2009, **280**, 226–234.
62 M. J. Frisch, G. W. Trucks, H. B. Schlegel, G. E. Scuseria, M. A. Robb, J. R. Cheeseman, G. Scalmani, V. Barone, G. A. Petersson, H. Nakatsuji,

Open Access Article. Published on 20 May 2024. Downloaded on 5/21/2024 8:27:22 AM.
This article is licensed under a Creative Commons Attribution 3.0 Unported Licence.

X. Li, M. Caricato, A. V. Marenich, J. Bloino, B. G. Janesko, R. Gomperts, B. Mennucci, H. P. Hratchian, J. V. Ortiz, A. F. Izmaylov, J. L. Sonnenberg, D. Williams-Young, F. Ding, F. Lipparini, F. Egidi, J. Goings, B. Peng, A. Petrone, T. Henderson, D. Ranasinghe, V. G. Zakrzewski, J. Gao, N. Rega, G. Zheng, W. Liang, M. Hada, M. Ehara, K. Toyota, R. Fukuda, J. Hasegawa, M. Ishida, T. Nakajima, Y. Honda, O. Kitao, H. Nakai, T. Vreven, K. Throssell, J. A. Montgomery Jr, J. E. Peralta, F. Ogliaro, M. J. Bearpark, J. J. Heyd, E. N. Brothers, K. N. Kudin, V. N. Staroverov, T. A. Keith, R. Kobayashi, J. Normand, K. Raghavachari, A. P. Rendell, J. C. Burant, S. S. Iyengar, J. Tomasi, M. Cossi, J. M. Millam, M. Klene, C. Adamo, R. Cammi, J. W. Ochterski, R. L. Martin, K. Morokuma, O. Farkas, J. B. Foresman and D. J. Fox, *Gaussian 16, Revision C.01*, Gaussian Inc., Wallingford, CT, 2016.

63 H.-J. Werner, P. J. Knowles, G. Knizia, F. R. Manby, M. Schütz, P. Celani, T. Korona, R. Lindh, A. Mitrushenkov, G. Rauhut, K. R. Shamasundar, T. B. Adler, R. D. Amos, A. Bernhardsson, A. Berning, D. L. Cooper, M. J. O. Deegan, A. J. Dobbyn, F. Eckert, E. Goll, C. Hampel, A. Hesselmann, G. Hetzer, T. Hrenar, G. Jansen, C. Köppl, Y. Liu, A. W. Lloyd, R. A. Mata, A. J. May, S. J. McNicholas, W. Meyer, M. E. Mura, A. Nicklass, D. P. O'Neill, P. Palmieri, K. Pflüger, R. Pitzer, M. Reiher, T. Shiozaki, H. Stoll, A. J. Stone, R. Tarroni, T. Thorsteinsson, M. Wang and A. Wolf, *MOLPRO, a Package of Ab Initio Programs (Version 2012)*, see: **http://www.molpro.net**.

64 H.-J. Werner, P. J. Knowles, G. Knizia, F. R. Manby and M. Schütz, *Wiley Interdiscip. Rev.: Comput. Mol. Sci.*, 2012, **2**, 242–253.

65 H.-J. Werner, P. J. Knowles, F. R. Manby, J. A. Black, K. Doll, A. Heßelmann, D. Kats, A. Köhn, T. Korona, D. A. Kreplin, Q. Ma, I. Miller, F. Thomas, A. Mitrushchenkov, K. A. Peterson, I. Polyak, G. Rauhut and M. Sibaev, *J. Chem. Phys.*, 2020, **152**, 144107.

66 E. Sicilia, G. Mazzone, A. Pérez-González, J. Pirillo, A. Galano, T. Heine and N. Russo, *Phys. Chem. Chem. Phys.*, 2017, **19**, 16178–16188.

67 K. K. Irikura, I. Goddard and A. William, *J. Am. Chem. Soc.*, 1994, **116**, 8733–8740.

68 N. Sändig and W. Koch, *Organometallics*, 1997, **16**, 5244–5251.

69 R. Otto, J. Brox, S. Trippel, M. Stei, T. Best and R. Wester, *Nat. Chem.*, 2012, **4**, 534–538.

70 J. Xie, R. Otto, J. Mikosch, J. Zhang, R. Wester and W. L. Hase, *Acc. Chem. Res.*, 2014, **47**, 2960–2969.

71 B. Bastian, T. Michaelsen, J. Meyer and R. Wester, *Astrophys. J.*, 2019, **878**, 162.

72 C. Heinemann, J. Schwarz and H. Schwarz, *Chem. Phys. Lett.*, 1995, **247**, 611–613.

73 O. W. Wheeler, M. Salem, A. Gao, J. M. Bakker and P. B. Armentrout, *Int. J. Mass Spectrom.*, 2019, **435**, 78–92.

74 F. J. Wensink, N. Roos, J. M. Bakker and P. B. Armentrout, *Inorg. Chem.*, 2022, **61**, 11252–11260.

75 J. Kozubal, T. Heck and R. B. Metz, *J. Phys. Chem. A*, 2020, **124**, 8235–8245.

76 R. Otto, J. Xie, J. Brox, S. Trippel, M. Stei, T. Best, M. R. Siebert, W. L. Hase and R. Wester, *Faraday Discuss.*, 2012, **157**, 41–57.

77 E. Carrascosa, M. Stei, M. A. Kainz and R. Wester, *Mol. Phys.*, 2015, **113**, 3955.